Taylor & Francis
Taylor & Francis Group

Vehicle System Dynamics
International Journal of Vehicle Mechanics and Mobility

ISSN: 0042-3114 (Print) 1744-5159 (Online) Journal homepage: https://www.tandfonline.com/loi/nvsd20

Predictive lateral control to stabilise highly automated vehicles at tire-road friction limits

Shengbo Eben Li, Hailiang Chen, Renjie Li, Zhengyu Liu, Zhitao Wang & Zhe Xin

To cite this article: Shengbo Eben Li, Hailiang Chen, Renjie Li, Zhengyu Liu, Zhitao Wang & Zhe Xin (2020) Predictive lateral control to stabilise highly automated vehicles at tire-road friction limits, Vehicle System Dynamics, 58:5, 768-786, DOI: 10.1080/00423114.2020.1717553

To link to this article: https://doi.org/10.1080/00423114.2020.1717553

VEHICLE SYSTEM DYNAMICS
2020, VOL. 58, NO. 5, 768–786
https://doi.org/10.1080/00423114.2020.1717553

Predictive lateral control to stabilise highly automated vehicles at tire-road friction limits

Shengbo Eben Li[a]*, Hailiang Chen[b]*, Renjie Li[a], Zhengyu Liu[a], Zhitao Wang[a] and Zhe Xin[b]

[a]State Key Lab of Automotive Safety and Energy, School of Vehicle and Mobility, Tsinghua University, Beijing, People's Republic of China; [b]Vehicle Engineering, China Agricultural University, Beijing, People's Republic of China

ABSTRACT

This paper proposes a linear predictive lateral control method to stabilise a highly automated vehicle (HAV) at the tire-road friction limits when tracking a (tight) desired path. Two approaches are adopted to linearise the vehicle model around the tire saturation region: (1) the lateral force of the front tire is selected as the control input instead of the steer angle and (2) the rear tire dynamics is locally linearised at the current operating point within the predictive horizon. The friction limits of both the front and rear tires are utilised to define an enveloped stable zone, which serves as the safety constraints for the predictive controller. Simulation results show that the proposed controller is able to stabilise a vehicle when tracking a tight desired path at a high speed even on a low-adhesion road. Moreover, the robustness of the proposed controller is also verified as it tolerates small estimation errors in the road friction coefficient.

ARTICLE HISTORY
Received 25 April 2019
Revised 18 December 2019
Accepted 19 December 2019

KEYWORDS
Automated vehicles; lateral control; predictive control; tire dynamics; optimisation

1. Introduction

Road vehicles have the potential to lose lateral stability when performing extreme manoeuvres, such as emergency obstacle avoidance, high-speed turning and driving on low-adhesion roads. Under these conditions, the lateral tire forces may reach the friction limits and become saturated, which is the leading cause of vehicle instability [1,2]. Such tire nonlinearities make the path tracking in extreme situations a difficult task for highly automated vehicles (HAVs).

To prevent vehicle instability in extreme path-tracking tasks, the first question to be answered is how to assess vehicle stability based on the observed vehicle state. The phase portrait method is commonly used to analyse vehicle stability by plotting a cluster of state trajectories from different initial conditions. Two types of phase planes have been adopted in previous studies: (1) sideslip angle at the centre of gravity (CG) β with its rate $\dot{\beta}$, i.e. $\beta - \dot{\beta}$ [3] and (2) sideslip angle β with yaw rate r, i.e. $\beta - r$ [4,5]. Inagaki et al. [3] experimentally depicted the state trajectories of different steady-state cornering conditions in the

CONTACT Shengbo Eben Li lisb04@gmail.com
* S. Li and L. Chen have equally contributed to this research.

$\beta - \dot{\beta}$ phase plane, and roughly determined the bounds of the stable zone through empirical analysis. With the development of on-board gyro technology, yaw rate r has become a measurable state for many commercialised vehicles, which arouses an increasing interest to analyse vehicle stability using the $\beta - r$ phase portrait. Ono et al. [4] revealed that vehicle instability is inherently caused by the state trajectory bifurcation around the saddle points in the $\beta - r$ phase plane, and pointed out that the saddle points emerge from the saturation of lateral tire forces. The stable and unstable zones can be hence identified based on the location of the saddle points. On the basis of Ono's finding, Gerdes and his leagues [2] defined a parallelogram-shaped stable zone in the $\beta - r$ phase plane, of which the upper and lower bounds are determined by the maximum yaw rate under the current tire-road friction limits, and the left and right bounds come from the constraint that the rear wheel slip angle stays within the non-saturation region. It has been demonstrated in [2] that this stable zone can stabilise a vehicle at the limits of handling. However, it has been found in [2] that there is a small overshoot in the yaw rate before the vehicle reaches the equilibrium state during steady-state cornering. Taking this into account, Gerdes et al. [5] further expanded the stable zone by combining the maximum and minimum real slip angles with the yaw acceleration nullclines determined by the maximum stable steering angle, which admits the yaw rate overshoot instability control.

After the stable zone is determined, the second question to be addressed is how to apply lateral control to confine the vehicle state within the stable zone when tracking a desired path. Model predictive control (MPC) is a popular approach to achieve such a goal [6], because it can explicitly handle constraints and optimise the path-tracking performance simultaneously [7]. Borrelli et al. [8] designed a predictive lateral controller using the Pacejka tire model to realise accurate path tracking. In this study, the vehicle stability is ensured by imposing a constraint on the front/rear tire slip angles. However, the introduction of the nonlinear tire model into the prediction equation results in a nonlinear model predictive control (NMPC) problem, which is inefficient to solve and thus difficult for real-time implementation. Yoon et al. [9] followed the nonlinear path-tracking method, but incorporated the online obstacle information into the model prediction process. To alleviate the computational burden caused by model nonlinearity, Falcone et al. [10] converted the nonlinear MPC to a linear time-varying problem by successively linearising the nonlinear vehicle model around a reference system trajectory. Although it manages to reduce the computational complexity to some extent, it requires to evaluate the Jacobians of the nonlinear vehicle model along the reference trajectory points within the predictive horizon, which is also time-consuming. Khajepour et al. [11] used a simplified linear bicycle model for MPC-based path tracking by assuming small tire slip angles. The state constraints on the yaw rate and sideslip angle were enforced to stabilise the vehicle for high-speed obstacle avoidance. However, this method cannot compensate for the tire nonlinearity if the vehicle encounters extreme situations in which the operating point of the tires are likely to move away from the linear region.

The main contribution of this paper is a linear predictive control method to stabilise HAVs at the handling limits when tracking a desired path. We mainly consider extreme situations where braking is not allowed (for example, a car on the adjacent lane is approaching fast behind when the ego vehicle is trying to avoid an emergency ahead; or the road surface has very low adhesion where braking may lock the wheels). This enables us to focus on the design of a lateral controller regardless of speed regulation. Unlike many previous

studies, e.g. [8,10,12], the lateral force of the front tire is selected as the control input to avoid model nonlinearity when the tires are working around the tire-road friction limits. After the optimal lateral force of the front tire is obtained, the steer angle input is recovered by numerically solving an inverse tire model. The friction limits of both the front and rear tires are used to define the enveloped zone for the yaw rate and sideslip angle, which are then enforced as the safety constraints in the predictive horizon.

The rest of this paper is organised as follows: Section 2 presents the vehicle model including a nonlinear tire model to be used throughout the paper. Section 3 analyses the vehicle lateral stability using the phase portrait method. Section 4 presents the predictive control method to track a desired path at the friction limits. Section 5 demonstrates the performance and robustness of the proposed control method by simulation. Section 6 concludes the paper.

2. Vehicle dynamics

2.1. Nonlinear vehicle lateral model

A single-track bicycle model [13] is used to describe the lateral dynamics of a vehicle, as shown in Figure 1. The bicycle model is derived by assuming: (1) the forces on left and right wheels are lumped together considering symmetry; (2) the longitudinal speed is assumed to be constant, and the pitch and roll motion are neglected; (3) the vehicle is rear-wheel drive, and the front wheels only serve as the steering wheels.

The dynamics of the single-track bicycle model are

$$\begin{aligned} mv(\dot{\beta} + r) &= F_{yf} + F_{yr} \\ I_{zz}\dot{r} &= aF_{yf} - bF_{yr}, \end{aligned} \tag{1}$$

where m is the vehicle mass, v is the longitudinal speed, I_{zz} is the moment of inertia, a and b are the distances of front and rear axle from CG, respectively, r is the yaw rate at CG, β is the vehicle sideslip angle at CG, F_{yf} and F_{yr} are the lateral tire forces of the front and rear tires, respectively.

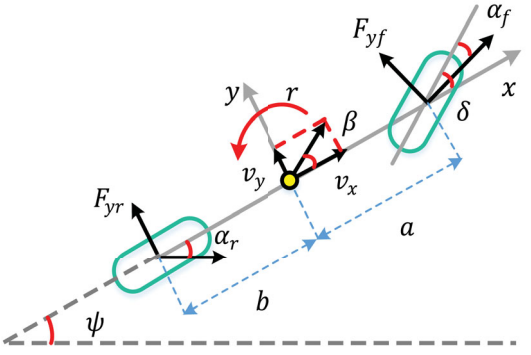

Figure 1. Single-track bicycle model.

To perform path tracking at the tire-road friction limits, a high-fidelity tire model is essential to provide accurate prediction of the tire behaviour. The Fiala tire model [2] is used here to approximate the relation between the lateral tire force and the tire slip angle:

$$F_{y\#} = \text{Tire}(\alpha_\#, \mu_\#) = \begin{cases} -C_\# \tan\alpha_\# \left(\dfrac{{C_\#}^2 (\tan\alpha_\#)^2}{27(\mu_\# F_{z\#})^2} - \dfrac{C_\# |\tan\alpha_\#|}{3\mu_\# F_{z\#}} + 1 \right) & |\alpha_\#| \le \alpha_{\max,\#} \\ -\mu_\# F_{z\#} \text{sgn}(\alpha_\#) & |\alpha_\#| > \alpha_{\max,\#} \end{cases} \tag{2}$$

where $C_\#$ is the tire cornering stiffness, $\alpha_\#$ is the tire slip angle, $F_{z\#}$ is the tire load, $\mu_\#$ is the lateral friction coefficient, and the subscript $\# \in \{f, r\}$ represents the front or rear tires.

The slip angles of the front and rear tires can be approximated from the geometric relationship between the front/rear axle and the CG:

$$\alpha_r = \beta - \frac{br}{v} \tag{3}$$

$$\alpha_f = \beta + \frac{ar}{v} - \delta, \tag{4}$$

where δ is the steer angle of the front wheel. The load transfer may occur when the vehicle is turning, thus changing the load distribution in the lateral direction. Here, we neglect the load transfer between the left and right wheels. Therefore, the loads on the front and rear tires are constant and calculated by

$$F_{zf} = \frac{b}{2(a+b)} mg \tag{5}$$

$$F_{zr} = \frac{a}{2(a+b)} mg, \tag{6}$$

where F_{zf} is the load of the front tire, and F_{zr} is the load of the rear tire, g is acceleration of gravity. We have assumed a rear-wheel-drive vehicle model, therefore its longitudinal traction force would occupy a part of the tire capability and the magnitude of the lateral friction limit of the rear wheel is slightly smaller than that of the front. Therefore, we should exclude the effect of the longitudinal tire force when calculating the lateral friction coefficient $\mu_\#$. For the front wheel, its lateral friction coefficient μ_f equals to the tire-road friction coefficient μ (we assume that the rolling resistance force is negligible). The lateral friction coefficient of the rear wheel μ_r is corrected by eliminating the longitudinal traction force [14]:

$$\mu_r = \frac{\sqrt{(\mu F_{zr})^2 - {F_{xr}}^2}}{F_{zr}}, \tag{7}$$

where F_{xr} is the longitudinal traction force of the rear tire. The notation $\alpha_{\max,\#}$ represents the tire slip angle when the tire fully-sliding behaviour occurs, approximated by

$$\alpha_{\max,\#} = \frac{3\mu_\# F_{z\#}}{C_\#}. \tag{8}$$

The maximum available lateral forces of the front and rear tires are the product of the lateral

Table 1. Parameters of vehicle model.

Parameter	Symbol	Value
Vehicle mass	m	1330 (kg)
Yaw moment of inertia	I_{zz}	1536 (kg/m^2)
Wheel base	L	2.91 (m)
Distance from mass centre to Front axle	a	1.015 (m)
Distance from mass centre to rear axle	b	1.895 (m)
Front wheel cornering stiffness	C_f	72,197 (N/rad)
Rear wheel cornering stiffness	C_r	39,930 (N/rad)

friction coefficient and the vertical tire load:

$$\begin{aligned} F_{yf,max} &= \mu_f F_{zf} \\ F_{yr,max} &= \mu_r F_{zr} \end{aligned} \tag{9}$$

The related vehicle model parameters used for this paper are listed in Table 1.

3. Vehicle stability analysis

The vehicle state may enter some inherent unstable zones during turning if the tire lateral forces are saturated. Therefore, we first identify the bounds of the vehicle stable zone by open-loop analysis, which could serve as the constraints on the vehicle state for us to design a stabilising predictive controller in the next section.

3.1. State trajectories under steady-state cornering conditions

We analyse the vehicle instability by using the $\beta - r$ phase portrait under the steady-state cornering conditions. The phase portrait is based on the single-track bicycle model assuming a constant longitudinal speed and a fixed steer angle:

$$\dot{\beta} = \frac{F_{yf} + F_{yr}}{mv} - r \tag{10a}$$

$$\dot{r} = \frac{aF_{yf} - bF_{yr}}{I_{zz}} \tag{10b}$$

$$F_{yf} = \text{Tire}(\beta, r, \mu_f) \tag{10c}$$

$$F_{yr} = \text{Tire}(\beta, r, \mu_r). \tag{10d}$$

Equations (10c) and (10d) are obtained by substituting (1) and (2) into (2). Figure 2 shows the phase portraits plotted at the steering angle $\delta = 0°, -3°, -8°, -12°$, the constant speed $v = 10$ m/s and the tire-road coefficient $\mu = 0.55$ from different initial conditions. In Figure 2(a), the stable equilibrium is marked by a red dot in the middle of the phase plane. There is a domain of attraction around the stable equilibrium, and all the trajectories starting within it will converge to the equilibrium even under certain disturbances. The two equilibria marked by a red triangle are unstable saddle points where bifurcation occurs and four unstable zones are formed. In the unstable zone ① and ④, vehicle instability is caused by large yaw rate; whereas in the unstable zone ② and ③, the instability is caused by a joint effect of a large sideslip angle and the yaw motion.

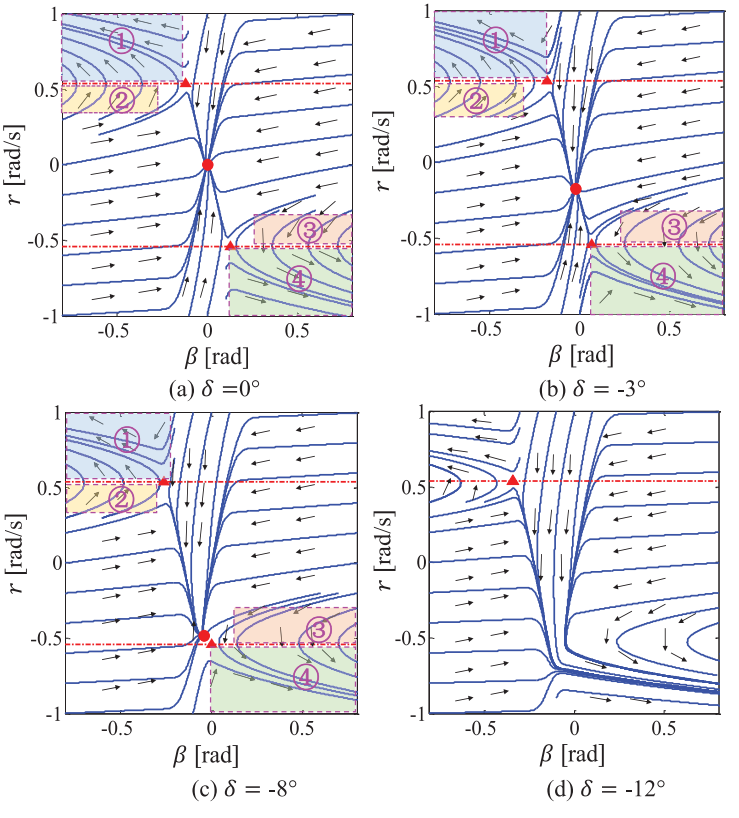

Figure 2. Phase plane representations of vehicle dynamics.

If the steer angle is increased to −3°, the stable equilibrium moves towards a larger (negative) sideslip angle and yaw rate, as shown in Figure 2(b); if the steer angle is increased to −8°, the stable equilibrium gets much closer to the saddle point (shown in Figure 2(c)), and any lateral disturbance to the vehicle would lead to instability; if the steer angle reaches −12°, the stable equilibrium disappears and the unstable zones are expanded to the whole phase plane, as shown in Figure 2(d). Note that the upper (lower) saddle points lie on a horizontal line (denoted by a red dash-dot line) at any steer angles. This property will be proved in the following section and can be used to constitute a stable zone.

3.2. Analysis of vehicle equilibrium state

Here we calculate the vehicle state, including the vehicle sideslip angle, yaw rate, lateral forces of the front and rear tires, at the equilibrium with given constant vehicle speed and tire-road coefficient. The equilibrium state is derived by setting $\dot{\beta} = 0$ and $\dot{r} = 0$ in the dynamic bicycle model:

$$mvr^{eq} = F_{yf}^{eq} + F_{yr}^{eq} \tag{11a}$$

$$aF_{yf}^{eq} - bF_{yr}^{eq} = 0 \tag{11b}$$

$$F_{yf}^{eq} = \text{Tire}(\beta^{eq}, r^{eq}, \mu_f) \tag{11c}$$

$$F_{yr}^{eq} = \text{Tire}(\beta^{eq}, r^{eq}, \mu_r), \tag{11d}$$

where the superscript '*eq*' represents 'equilibrium'. F_{yf}^{eq} and F_{yr}^{eq} are functions of β^{eq} and r^{eq}. Because there are four variables and four equations, we can solve the equilibrium state using the vehicle speed, tire-road coefficient, and steer angle.

We plot the vehicle equilibrium state with respect to the steer angle at $v = 10$ m/s and $\mu = 0.5$ as shown in Figure 3, by setting $\dot{\beta} = 0$ and $\dot{r} = 0$ in the dynamic bicycle model. There are two kinds of equilibria: the first kind of equilibria is marked by red dots in Figure 3. At these equilibria, β^{eq} slowly increases with a larger steer angle δ (see Figure 3(a)), and the yaw rate increases accordingly (see Figure 3(b)). Furthermore, the lateral forces of the front and rear tires are not saturated at these equilibria because they do not exceed the tire friction limits (denoted by the blue dashed lines), as shown in Figure 3(c) and Figure 3(d). Hence, we can conclude that these equilibria correspond to the steady state of normal cornering conditions.

Similarly, let us discuss the properties of the second kind of equilibria that are marked by red triangles (saddle points). From Figure 3(d), we can see that F_{yr}^{eq} is saturated and hence constant at these equilibria and F_{yf}^{eq} is nearly saturated and also constant because it is proportional to F_{yr}^{eq} according to (11b). If the steer angle increases, β^{eq} would increase dramatically, and there is counter steer as r^{eq} and the steer angle have opposite signs. In

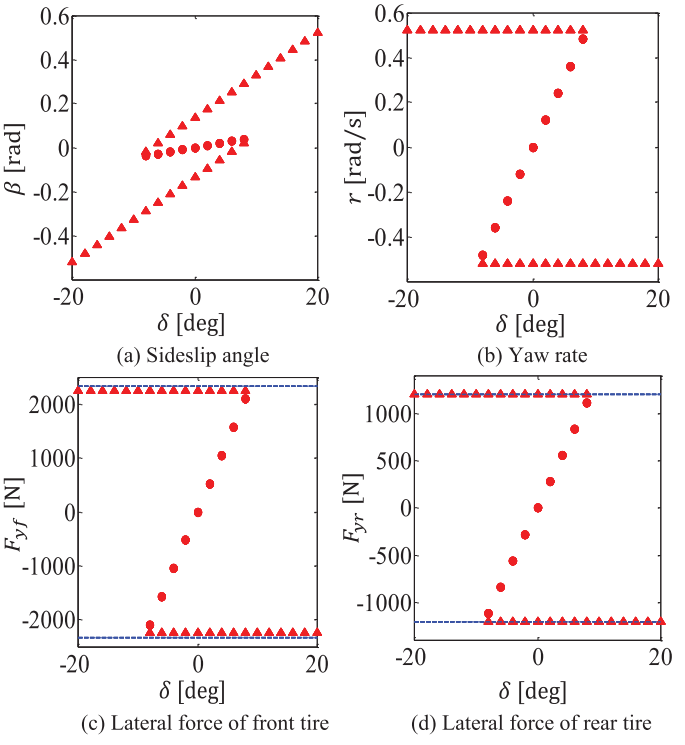

Figure 3. Equilibria analysis of the bicycle model.

this situation, the rear tire gets saturated first as $\mu_r < \mu_f$ and has a slightly small friction limit. Therefore, the friction limit of the rear tire decides the maximum driving capability that a vehicle can achieve.

3.3. Bounds for vehicle stable zone

Now let us show that the upper (lower) saddle points lie on a horizontal line. This statement can be simply proved by showing that r^{eq} is constant for the upper (lower) unstable equilibria. According to Section 3.2, F_{yf}^{eq} and F_{yr}^{eq} are constant at these equilibria because the rear tire is saturated. Therefore, from (9a) we know that r^{eq} is also constant. This constant r^{eq} can be seen as the maximum allowed yaw rate $r_{\max}$, calculated by setting $F_{yr}^{eq} = \mu_r F_{zr}$ in Equation (11a):

$$r_{\max} = \frac{\mu_r F_{zr} + b\mu_r F_{zr}/a}{mv} = \frac{\mu_r g}{v}. \tag{12}$$

Hence, the yaw rate at the CG should be constrained by

$$-\frac{\mu_r g}{v} \le r \le \frac{\mu_r g}{v}. \tag{13}$$

Besides the yaw rate, we should also restrict the vehicle sideslip angle because of the existence of the unstable zones ② and ③ in the phase plane (see Figure 2). This can be achieved by restricting the slip angle of rear tire between their peak values:

$$-\alpha_{\max,r} \le \alpha_r \le \alpha_{\max,r}. \tag{14}$$

Substituting (1) into (11), we have

$$-\alpha_{\max,r} \le \beta - \frac{br}{v} \le \alpha_{\max,r}. \tag{15}$$

Rearranging (13), we have the constraint:

$$\frac{br}{v} - \alpha_{\max,r} \le \beta \le \frac{br}{v} + \alpha_{\max,r}. \tag{16}$$

Finally, we construct the stable zone by constraints (11) and (14) in the $\beta - r$ phase plane. The stable zone should be updated in real time because its bounds vary with the vehicle speed and the tire-road friction coefficient. More specifically, the upper and lower bounds are proportional to μ/v according to (10). The locations of the left and right bounds are influenced by the tire-road coefficient according to (14). A smaller tire-road coefficient and higher vehicle speed would shrink the stable zone and make the vehicle prone to instability. This stable zone can be taken as the safety envelope of the predictive path-tracking controller.

4. Controller design

This section designs a predictive lateral controller for accurate path tracking at the tire-road friction limits. It is assumed that an upper-level path planner would generate a desired path according to the road environment. At each control step, an open-loop optimal control problem is formulated subject to a linearised vehicle model and the safety envelope.

4.1. Model linearisation for controller design

To linearise the vehicle model given in Section 2, we must cope with the nonlinearity originated from the lateral tire forces F_{yf} and F_{yr}. For the lateral force of the front tire F_{yf}, we can directly assign it as the control input [2], because it can be controlled by solving the desired steer angle input δ_{des} from the tire model (2) and Equation (2) given the on-board measurement of sideslip angle β, yaw rate r, longitudinal speed v, and the estimated μ. This partition approach can preserve the nonlinearity of the front tire and admit a linear relation between the input and state in the vehicle dynamics. However, the lateral force of the rear tire F_{yr} cannot be treated in the same way because it is not directly controllable. Therefore, we have to linearise F_{yr} locally at the current operating point and substitute it into the prediction model. This local linearisation is based on the first-order Taylor expansion of the nonlinear tire model $F_{yr} = \text{Tire}(\alpha_r, \mu_r)$ around the current rear slip angle:

$$F_{yr} \approx \bar{F}_{yr} - \tilde{C}_{r,\bar{\alpha}_r}(\alpha_r - \bar{\alpha}_r), \tag{17}$$

where $\bar{\alpha}_r$ is the current rear slip angle, $\bar{F}_{yr} = \text{Tire}(\bar{\alpha}_r, \mu_r)$ is the current lateral force of the rear tire, and $\tilde{C}_{r,\bar{\alpha}_r} = \partial \text{Tire}(\alpha_r, \mu_r)/\partial \alpha_r|_{\alpha_r = \bar{\alpha}_r}$ is the local cornering stiffness After such manipulations on F_{yf} and F_{yr}, the vehicle dynamics can be described by

$$\begin{aligned} \dot{\beta} &= \frac{F_{yf} + \bar{F}_{yr} - \tilde{C}_{r,\bar{\alpha}_r}(\alpha_r - \bar{\alpha}_r)}{mv} - r \\ \dot{r} &= \frac{aF_{yf} - b(\bar{F}_{yr} - \tilde{C}_{r,\bar{\alpha}_r}(\alpha_r - \bar{\alpha}_r)}{I_{zz}}. \end{aligned} \tag{18}$$

Substituting (1) into (16) yields

$$\begin{aligned} \dot{\beta} &= \frac{F_{yf} + \bar{F}_{yr} - \tilde{C}_{r,\bar{\alpha}_r}\left(\beta - \frac{br}{v} - \bar{\alpha}_r\right)}{mv} - r \\ \dot{r} &= \frac{aF_{yf} - b(\bar{F}_{yr} - \tilde{C}_{r,\bar{\alpha}_r}\left(\beta - \frac{br}{v} - \bar{\alpha}_r\right)}{I_{zz}}. \end{aligned} \tag{19}$$

Therefore, a local linear time-invariant model is obtained as

$$\begin{aligned} \dot{x}(t) &= Ax(t) + Bu(t) + d(t) \\ z(t) &= Cx(t), \end{aligned} \tag{20}$$

where $x(t) = [y(t), \psi(t), \beta(t), r(t)]^T$ and

$$A = \begin{bmatrix} 0 & v & v & 0 \\ 0 & 0 & 0 & 1 \\ 0 & 0 & \dfrac{-\tilde{C}_{r,\bar{\alpha}_r}}{mv} & \dfrac{b\tilde{C}_{r,\bar{\alpha}_r}}{mv^2} - 1 \\ 0 & 0 & \dfrac{b\tilde{C}_{r,\bar{\alpha}_r}}{I_{zz}} & \dfrac{-b^2\tilde{C}_{r,\bar{\alpha}_r}}{vI_{zz}} \end{bmatrix}, B = \begin{bmatrix} 0 \\ 0 \\ \dfrac{1}{mv} \\ \dfrac{a}{I_{zz}} \end{bmatrix},$$

$$d(t) = \begin{bmatrix} 0 \\ 0 \\ \dfrac{\bar{F}_{yr} + \tilde{C}_{r,\bar{\alpha}_r}\bar{\alpha}_r}{mv} \\ \dfrac{-b(\bar{F}_{yr} + \tilde{C}_{r,\bar{\alpha}_r}\bar{\alpha}_r)}{I_{zz}} \end{bmatrix}, C = \begin{bmatrix} 1\,0\,0\,0 \\ 0\,1\,0\,0 \end{bmatrix},$$

where y is the lateral displacement, ψ is the yaw angle, $z = [y, \psi]^T$ is the output for path tracking. Here, we take the desired lateral force of front tire as the control input $u = F_{yf,des}$. The matrices A and B are constant, and d is a disturbance input associated with the current vehicle state.

4.2. Formulation of lateral predictive controller

In automated driving applications, there is usually a local reference path for the motion controller to track. Assuming that the reference path is known, we can construct the following open-loop optimal control problem [15,16] for the stabilising MPC controller:

$$J = \int_t^{t+T} (\| z(\tau) - z_{ref}(\tau) \|_{\mathcal{Q}}^2 + \| u(\tau) \|_{\mathcal{R}}^2 + \rho_r \cdot {\epsilon_r}^2 + \rho_\alpha \cdot {\epsilon_\alpha}^2) d\tau, \tag{21}$$

subject to (18) and the safety envelope: (19a)

$$-F_{yf,max} \leq u(\tau) \leq F_{yf,max} \tag{22a}$$

$$\begin{bmatrix} 0 & 0 & 1 & -b/v \\ 0 & 0 & 0 & 1 \end{bmatrix} |x(\tau)| \leq \begin{bmatrix} r_{\max} + \epsilon_r \\ \alpha_{\max,r} + \epsilon_\alpha \end{bmatrix} \tag{22b}$$

$$\epsilon_r \geq 0 \tag{22c}$$

$$\epsilon_\alpha \geq 0, \tag{22d}$$

where t is the current control time, T is the prediction horizon, z_{ref} is the reference trajectory extracted from the reference path considering the current vehicle position and speed, $u = F_{yf,des}$ is the predicted control input, ϵ_α and ϵ_r are slack variables. The first term in the cost function penalises the path-tracking error by a weighting matrix $\mathcal{Q}$ of dimension 2×2; the second term penalises the magnitude of control input by a weighting matric $\mathcal{R}$ of dimension 1×1 (a scalar); and the last two terms introduce penalty on the stable bounds violation. Constraint (22a) represents the friction limit of the front tire, and constraint (22b) confines the vehicle state into the stable zone that has been introduced in Section 3.

4.3. Reverse calculation of desired steer angle

The optimal control input from MPC is the desired lateral force of the front tire $F_{yf,des}$, which cannot be directly sent to the vehicle. Therefore, the desired steer angle δ_{des} should be recovered by an inverse tire model which is derived from the tire model (2). Then, δ_{des}

is obtained by combining the inverse tire model with (2) as

$$\delta_{des} = \beta + \frac{ar}{v} - \text{Tire}^{-1}(F_{yf,des}). \tag{23}$$

Because (2) can be seen as a cubic polynomial with respect to $\tan\alpha_f$, it is easy to first find $\tan\alpha_{f,des}$ using a standard cubic formula and then get $\alpha_{f,des}$ through the inverse tangent function. There is a unique solution to (23) because the tire is operating in the non-saturation region which is ensured by constraint (22a).

5. Simulation results and validation

Simulations are performed on a Simulink/CarSim. It should be noted that although the MPC controller is derived under some simplifying assumptions, the CarSim vehicle model is based on real-car dynamics, which could make the simulation results more convincing. The MPC problem is numerically solved by using the YALMIP toolbox with the Gurobi solver [17]. The MPC controller parameters for simulation are shown in Table 2.

5.1. Simulation setting

The CarSim built-in double lane change (DLC) and tight double lane change (TDLC) are selected as the simulation scenarios to represent normal/emergent lane-change or obstacle-avoidance manoeuvres, whose reference paths are shown in Figure 4(a) and Figure 6(a). The simulations are conducted under four conditions, i.e. normal ($v = 55$ km/h, $\mu = 0.85$, DLC), tight ($v = 55$ km/h, $\mu = 0.85$, TDLC), low road adhesion ($v = 55$ km/h, $\mu = 0.5$, DLC), and high speed (v =75 km/h, μ =0.85, DLC), to showcase the path-tracking performance and stability of the designed MPC controller under different conditions. For comparison, the CarSim built-in optimal preview controller (OPC) is used as the benchmark. The OPC is based on MacAdam's work [18] which is very much like a standard linear MPC controller except that: (1) it employs a linear vehicle model that does not consider tire nonlinearity at tire-road friction limits and (2) it does not impose any safety constraints on the vehicle state to prevent instability.

5.2. Simulation results and analysis

Figure 4 shows the simulation results under the normal condition. The proposed MPC controller shows a better tracking performance than the OPC controller, as shown in Figure 4(a). Figure 4(b–d) give the steer angle profile, adhesion utilisation of the front and

Table 2. Predictive controller parameters.

Parameters	Symbols	Values
Predictive horizon	N	50
Sampling time	T_s	0.02 s
Tracking error penalising matrix	Q	$[10^4\ 0; 0\ 10^3]$
Input slew rate penalising matrix	R	0.01
Slip angle overshoot penalising factor	ρ_α	5×10^5
Yaw rate overshoot penalising factor	ρ_r	5×10^5

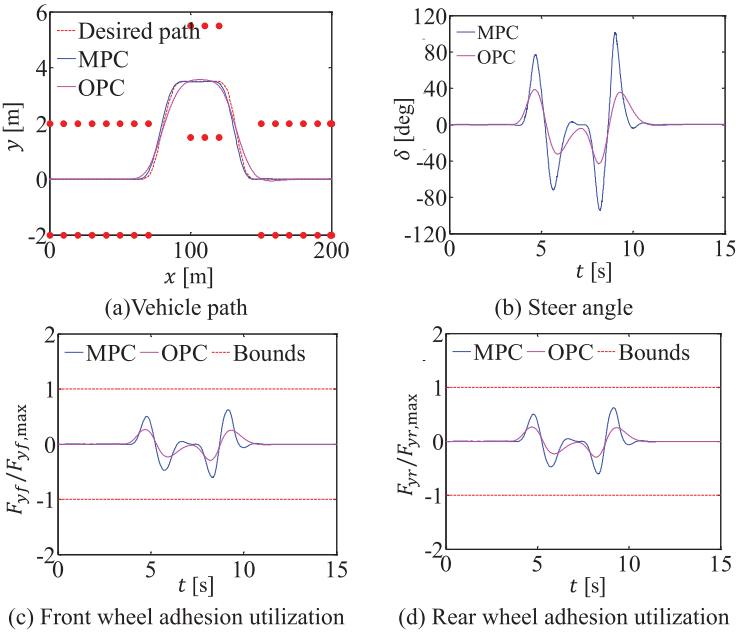

Figure 4. Normal condition ($v = 55$km/h, $\mu = 0.85$, DLC).

rear tires (adhesion utilisation is defined as the ratio of actual lateral tire force to the maximum available lateral tire force), respectively. In Figure 4(c,d), the front and rear adhesion utilisations being smaller than 1 means that both tires are not saturated. The $\beta - r$ trajectories are plotted in Figure 5, which shows that both controllers are enveloped in the stable zone. This result demonstrates that under normal conditions the proposed MPC controller outperforms the OPC controller slightly in the sense of a smaller path-tracking error, but the stability margin (indicated by the distance from the vehicle state to the stable zone boundaries) and riding comfort (indicated by steering angles and lateral forces) are somewhat sacrificed. Thus, it is hard to say that the MPC controller shows any advantages over OPC in normal driving conditions.

Figure 6 shows the simulation results under the tight condition. From Figure 6(a) we can see that the OPC tracks better initially, but eventually destabilises the vehicle. Figure 6(c,d) demonstrates that under OPC both the front and rear tire reach the friction limits and tire sliding occurs. Figure 7 shows that the $\beta - r$ trajectory of the OPC escapes the stable zone eventually. Compared with the OPC, the proposed MPC controller can actively restrict the tire slip angles and the vehicle state in advance, thereby preventing vehicle instability. These properties are reflected in Figures 6(b–d) and 7. We can also find in Figure 7 that the $\beta - r$ trajectory of the MPC controller would temporarily cross the lower bound. This is permitted by the slack variable ϵ_r but large deviation from the stable bounds is penalised. Compared with normal conditions, the MPC controller would sacrifice path-tracking performance to maintain vehicle stability when tracking a tight desired path.

Figures 8 and 9 present the simulation results under the low-adhesion condition. In these situations, the proposed MPC controller also reveals a better tracking performance

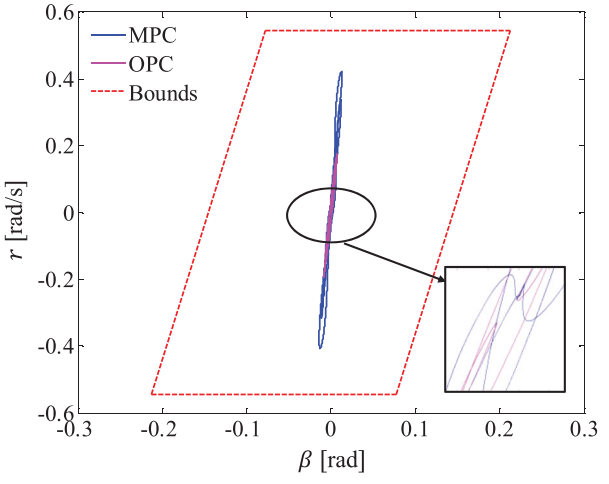

Figure 5. State trajectories under the normal condition.

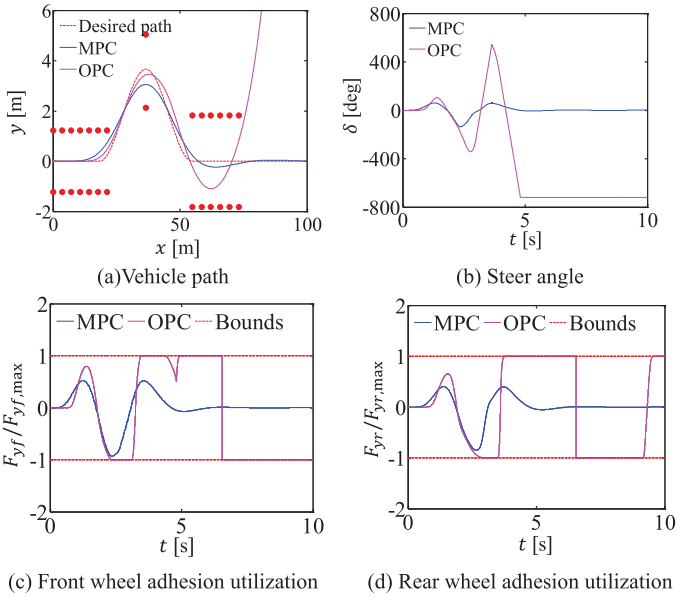

Figure 6. High-speed condition ($v = 55$ km/h, $\mu = 0.85$, TDLC).

than the OPC controller. The lateral forces of the front and rear tires are within friction limits under both controllers (shown in Figure 8(c,d)). The vehicle state trajectories are shown in Figure 9 and certainly are enveloped into a stable region. Compared with the normal condition, a slightly poor tracking performance is presented, however, the bounds of the stable region have changed dramatically in which case lower adhesion shrink the lower and upper bounds of the stable region, indicated by Equation (11). Thus, a stronger constraint on yaw rate during steering are presented in the MPC-based path tracking problem and the solved steer angle is smaller than the normal condition to satisfy the yaw rate constraints, shown in Figure 8(b).

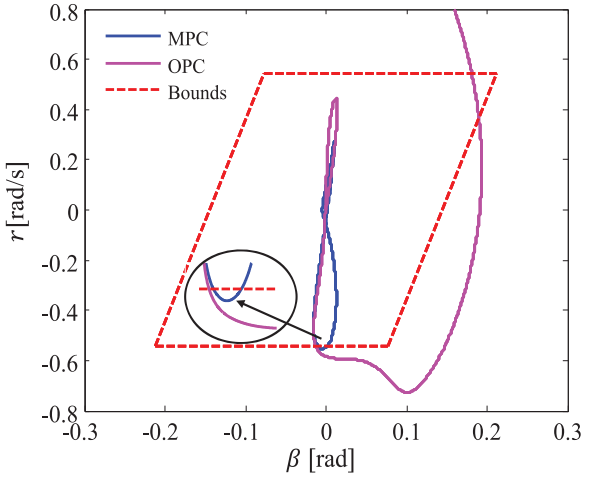

Figure 7. State trajectories for the tight condition.

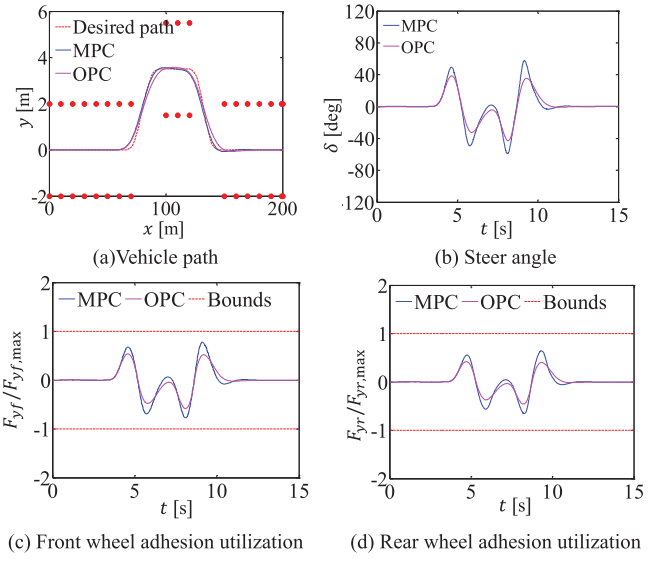

Figure 8. Low-adhesion condition ($v = 55$ km/h, $\mu = 0.5$, DLC).

Figures 10 and 11 present the simulation results under the high-speed condition. Under the high-speed condition, the MPC controller shows a smaller tracking error than the OPC controller and the adhesion utilisation is smaller than 1. Vehicle states are still confined to a stable region. Compared with the normal condition, the tracking performance is worse than the normal condition. The bounds of the stable region also changed, in which case high speed shrink both the four bounds of the stable region, indicated by Equations (11) and (14). The solved steer angle is also smaller than the normal condition to satisfy the constraints of yaw rate and rear tire slip angle, shown in Figure 10(b).

Figure 12 illustrates the maximum tracking error of the proposed MPC controller output by simulation under different road friction coefficient, vehicle speed and desired path

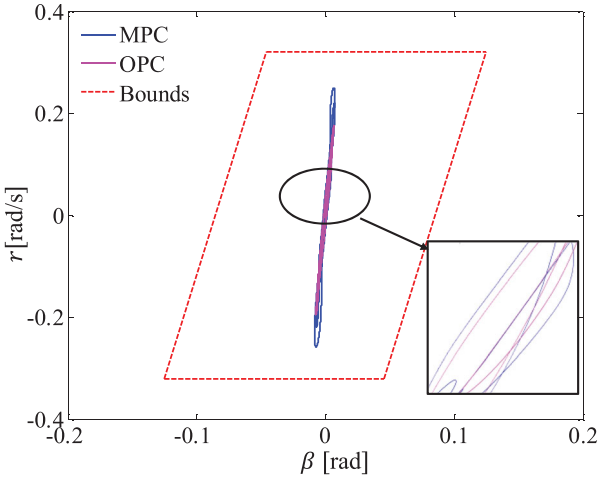

Figure 9. State trajectories for the low-adhesion condition.

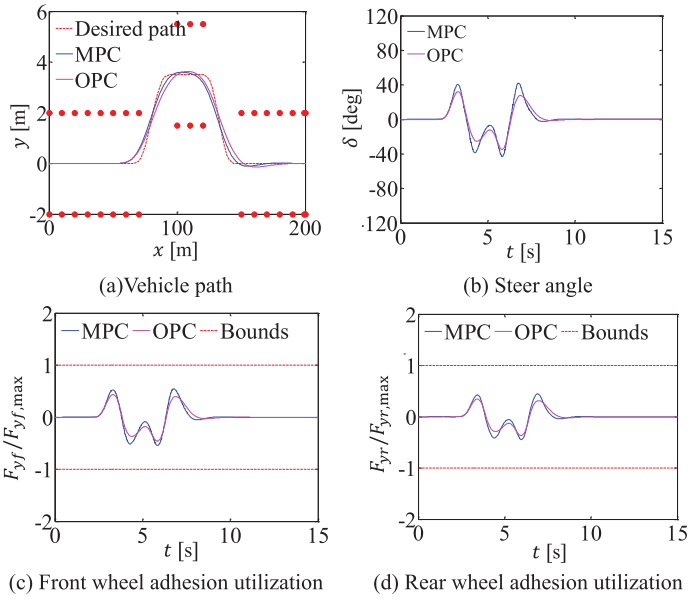

Figure 10. High-speed condition ($v = 75$ km/h, $\mu = 0.85$, DLC).

type (DLC/TDLC). Under the DLC reference path, the tracking performance goes down slowly when the road friction coefficient μ decreases from 0.8 to 0.4 but worsens rapidly once μ is below 0.4. This indicates that the proposed MPC controller is insensitive to road friction coefficient in normal lane change manoeuvres unless beyond normal range ($\mu <$ 0.4). In terms of vehicle speed, it is shown in Figure 12 that the path-tracking error of the proposed MPC would increase as the vehicle speed goes up from 40 to 70 km/h assuming a constant road friction coefficient μ. Compared with the DLC path, the TDLC path would produce relatively larger tracking error under the same configuration. This implies that the

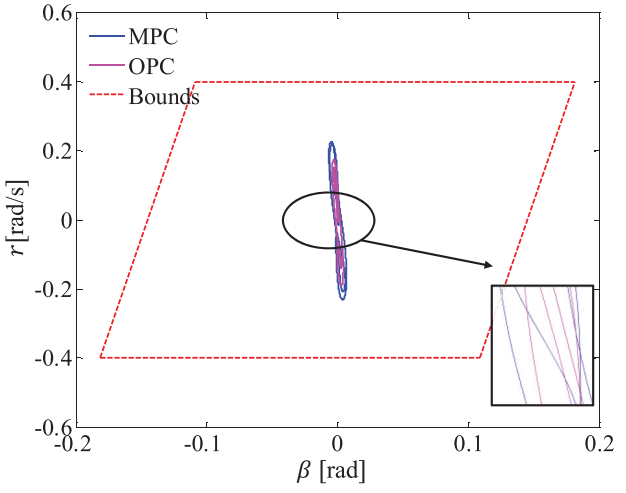

Figure 11. State trajectories for the high-speed condition.

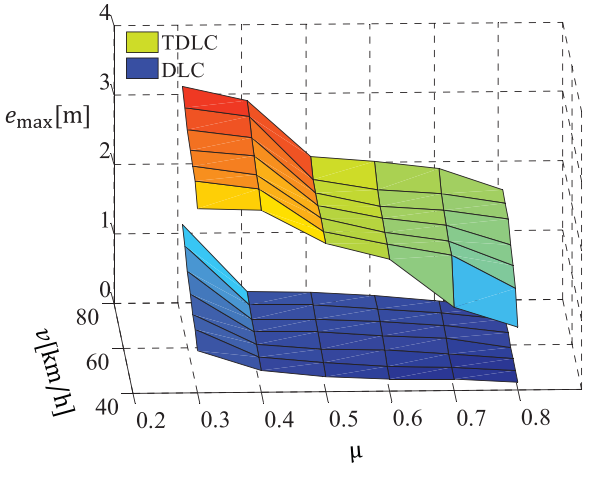

Figure 12. Tracking error under different conditions.

manoeuvrability of the reference path has a huge impact on the controller's performance: under circumstances that the environment constraints are tight, a good path-tracking controller itself is not sufficient, we need to manipulate the reference path as well to pursue a better performance.

To summarise, the proposed MPC path-tracking controller performs better under middle-speed range and loose environment constraints. On top of that, the controller does not appear to be influenced by the road friction coefficient μ if it is within normal range ($\mu \geq 0.4$) in normal lane change manoeuvres. However, if the road constraints become tight, the impact of μ on the controller's performance would become significant.

Since tire-road friction coefficients are hard to estimate in real applications, we hereby investigate the robustness of the proposed MPC controller in the presence of a friction coefficient estimation error. Figure 13 shows the maximum path-tracking error of the MPC

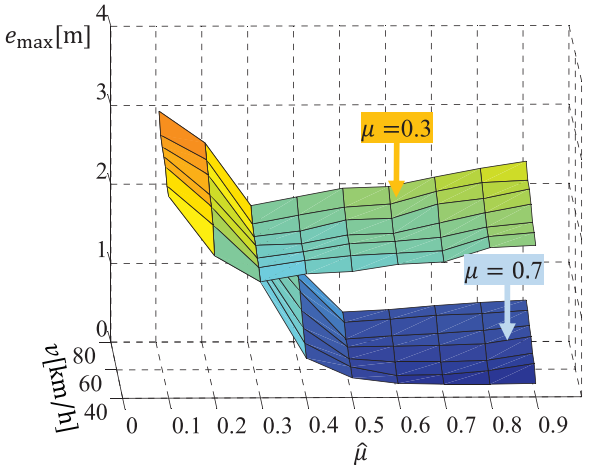

Figure 13. Robustness under a friction coefficient estimation error.

controller under different estimate of μ (denoted by $\hat{\mu}$) when the true μ are 0.7 and 0.3, respectively (the DLC scenario is used). When the true μ is 0.7, the maximum tracking error can be restricted fairly under 0.4 m when the estimated road friction limit $\hat{\mu}$ falls in the range of 0.5–0.9. However, if $\hat{\mu}$ falls below 0.5, the tracking performance deteriorates rapidly as $\hat{\mu}$ goes down. If the true μ is 0.3, the tracking performance is averagely worse than the case of $\mu = 0.3$. We can notice that in the low-road-adhesion situation the best path-tracking performance is achieved when $\hat{\mu}$ equals and either overestimate or underestimate of μ would undermine vehicle stability. From Figure 13, we can see that an unreasonable underestimate of μ would cause more severe result than overestimating it, no matter where the true μ lies.

In general, the proposed MPC path-tracking controller shows robustness when the road is normal (true μ is large) if the estimate $\hat{\mu}$ is not too far below the true μ. If the road is of low adhesion, the controller's robustness is impaired as either an overestimate or an underestimate would enlarge the maximum tracking error. The simulation result enlightens us that in such a case an overestimate is more bearable than an underestimate. That is to say, it should be avoided to estimate μ into an unreasonable region (< 0.3) when we use the proposed MPC controller.

6. Conclusion

This paper proposes a predictive lateral control method to stabilise an HAV at the tire-road friction limits when following a desired path. The nonlinear saturation property of the front tire is compensated for by an inverse model, thus allowing to directly use the lateral force of front tire as the control input. This design, together with linearised rear tire dynamics at the current operating point, yields a linear open-loop optimal control problem. The friction limits of both the front and rear tires are utilised to define the enveloped zone for vehicle yaw rate and sideslip angle, which is then enforced as the safety constraints in the predictive horizon. The simulation results demonstrate that: (1) under extreme conditions, the proposed predictive controller is able to improve vehicle stability at the cost of a compromised

tracking performance and (2) when working at different reference path configurations and vehicle speed, the method is robust in the sense that it tolerates an estimation error in the road friction coefficient μ. It should be noted that the electronic stability control (ESC) is not considered in the study, because ESC works in a different way to improve vehicle stability by applying braking to individual wheels to adjust vehicle motion (mainly yaw rate γ). We would anticipate that the proposed MPC path-tracking controller can achieve better stabilisation effect and path-tracking performance with the assistance of ESC under even extremer conditions, and look forward to conducting related research in the future.

Disclosure statement

No potential conflict of interest was reported by the authors.

Funding

This research is supported by the Beijing Natural Science Foundation with JQ18010, National Science Foundation of China with 51622504 and U1664263.

References

[1] Siampis E, Velenis E, Gariuolo S, et al. A real-time nonlinear model predictive control strategy for stabilization of an electric vehicle at the limits of handling. IEEE Trans Control Syst Technol. 2017: 1–13.
[2] Beal C, Gerdes J. Model predictive control for vehicle stabilization at the limits of handling. IEEE Trans Control Syst Technol. 2013;21(4):1258–1269.
[3] Inagaki S, Kshiro I, Yamamoto M. Analysis on vehicle stability in critical cornering. Proc Int Symp Adv Veh Contr. 1994;9(438 411):287–292.
[4] Ono E, Hosoe S, Tuan HD, et al. Bifurcation in vehicle dynamics and robust front wheel steering control. IEEE Trans Control Syst Technol. 1998;6(3):412–420.
[5] Bobier C, Gerdes J. Staying within the nullcline boundary for vehicle envelope control using a sliding surface. Veh Syst Dyn. 2013;51(2):199–217.
[6] Li S, Li K, Rajamani R, et al. Model predictive multi-objective vehicular adaptive cruise control. IEEE Trans Control Syst Technol. 2011;19(3):556–566.
[7] Li S, Gao F, Cao D, et al. Multiple-model switching control of vehicle longitudinal dynamics for platoon-level automation. IEEE Trans Veh Technol. 2016;65(6):4480–4492.
[8] Falcone P, Tseng H, Asgari J, et al. Integrated braking and steering model predictive control approach in autonomous vehicles. IFAC Proc Volumes. 2007;40(10):273–278.
[9] Yoon Y, Shin J, Kim H, et al. Model-predictive active steering and obstacle avoidance for autonomous ground vehicles. Control Eng Pract. 2009;17(7):741–750.
[10] Falcone FB, Tseng H, Asgari J, et al. Linear time-varying model predictive control and its application to active steering systems: stability analysis and experimental validation. Int J Robust Nonlinear Control. 2008;18(8):862–875.
[11] Ji J, Khajepour A, Melek W, et al. Path planning and tracking for vehicle collision avoidance based on model predictive control with multiconstraints. IEEE Trans Veh Technol. 2017;66(2):952–964.
[12] Raffo G, Gomes G, Normey-Rico J, et al. A predictive controller for autonomous vehicle path tracking. IEEE Trans Intell Transp Syst. 2009;10(1):92–102.
[13] Rajamani R. Vehicle dynamics and control. New York: Springer Science & Business Media; 2011.
[14] Hindiyeh R, Gerdes J. A controller Framework for autonomous drifting: design, stability, and experimental validation. J Dyn Syst Meas Control. 2014;136(5):051015.

[15] Eben S, Li KL, Wang J. Economy-oriented vehicle adaptive cruise control with coordinating multiple objectives function. Veh Syst Dyn. 2013;51(1):1–17.
[16] Zheng Y, Li S, Li K, et al. Distributed model predictive control for heterogeneous vehicle platoons under unidirectional topologies. IEEE Trans Control Syst Technol. 2017;25(3):899–910.
[17] Löfberg J. Modeling and solving uncertain optimization problems in YALMIP. IFAC Proc Volumes. 2008;41(2):1337–1341.
[18] MacAdam CC. Application of an optimal preview control for simulation of closed-loop automobile driving. IEEE Trans Syst Man Cybern. June 1981;11.